Submolecular Resolution by Variation of the Inelastic Electron Tunneling Spectroscopy Amplitude and its Relation to the AFM/STM Signal

Bruno de la Torre,[1,2,*] Martin Švec,[1,2] Giuseppe Foti,[1] Ondřej Krejčí,[1,3] Prokop Hapala,[1] Aran Garcia-Lekue,[4,5] Thomas Frederiksen,[4,5] Radek Zbořil,[2] Andres Arnau,[4] Héctor Vázquez,[1] and Pavel Jelínek[1,2,4,†]

[1]*Institute of Physics, Academy of Sciences of the Czech Republic, v.v.i., Cukrovarnická 10, 162 00 Prague, Czech Republic*
[2]*Regional Centre of Advanced Technologies and Materials, Palacký University, Šlechtitelů 27, 78371 Olomouc, Czech Republic*
[3]*Faculty of Mathematics and Physics, Department of Surface and Plasma Science, Charles University, V Holešovičkách 2, 180 00 Prague, Czech Republic*
[4]*Donostia International Physics Center (DIPC), Paseo Manuel Lardizabal 4, E-20018 San Sebastian, Spain*
[5]*Ikerbasque, Basque Foundation for Science, 48013 Bilbao, Spain*

(Received 29 June 2017; revised manuscript received 11 August 2017; published 16 October 2017)

Here we show scanning tunneling microscopy (STM), noncontact atomic force microscopy (AFM), and inelastic electron tunneling spectroscopy (IETS) measurements on an organic molecule with a CO-terminated tip at 5 K. The high-resolution contrast observed simultaneously in all channels unambiguously demonstrates the common imaging mechanism in STM/AFM/IETS, related to the lateral bending of the CO-functionalized tip. The IETS spectroscopy reveals that the submolecular contrast at 5 K consists of both renormalization of vibrational frequency and variation of the amplitude of the IETS signal. This finding is also corroborated by first principles simulations. We extend accordingly the probe-particle AFM/STM/IETS model to include these two main ingredients necessary to reproduce the high-resolution IETS contrast. We also employ the first principles simulations to get more insight into a different response of frustrated translation and rotational modes of the CO tip during imaging.

DOI: 10.1103/PhysRevLett.119.166001

The development of high-resolution scanning tunneling microscopy (STM) [1], atomic force microscopy (AFM) [2], and inelastic electron tunneling spectroscopy (IETS) [3] imaging with functionalized tips has allowed us to reach unprecedented spatial resolution of organic molecules on surfaces. Using these techniques, the chemical structure of molecules can be now routinely determined directly from experimental images [4,5], as well as the information about bond order [6], intermediates, and products of on-surface chemical reactions [7] or charge distribution within molecules [8].

The origin of the high-resolution AFM/STM imaging is now well understood within the framework of the so-called probe-particle (PP) model [9–11]. In general, an atom or molecule (the probe particle) placed at the tip apex is sensitive to spatial variations of the potential energy landscape of the molecule resulting from the interplay between Pauli, electrostatic, and van der Waals interactions [9,10,12,13]. At close tip-sample distances, the probe particle relaxes according to the potential energy surface, which gives rise to a sharp submolecular contrast. Nevertheless, neither direct experimental evidence nor a unified description of the imaging mechanism for all three scanning modes has been presented.

On one hand, noncontact AFM is most often used in the high-resolution imaging mode, which provides the highest spatial resolution with relatively straightforward interpretation, compared to the other two modes. This implies that the instrument operates in the frequency modulation (FM) mode [14], which is not a trivial task from both the instrumental and data acquisition point of view. From this perspective, the STM mode seems to be a more feasible choice. On the other hand, the interpretation of high-resolution STM images is not at all straightforward because of the convolution of the geometric and electronic effects [11]. The IETS mode [15] thus represents a promising alternative [3], but the high-resolution contrast was so far only demonstrated at sub-Kelvin temperatures. This temperature requirement poses severe limitations for its wider application.

In this Letter, we present simultaneous AFM/STM/IETS measurements of iron(II) phtalocyanine (FePc) on Au(111) acquired with a CO-terminated tip at 5 K [16]. These measurements (i) demonstrate that high-resolution IETS imaging is also feasible with standard LHe bath cryostats, and (ii) experimentally confirm the common imaging mechanism for all three imaging modes. Atomistic simulations using nonequilibrium Green's functions (NEGF) [27] and an extension of the PP model [3,10,16] provide a characterization of the contrast in the inelastic signal and a unified description of AFM/STM/IETS.

Figure 1(a) shows a constant-current STM image of coadsorbed FePc and CO molecules on Au(111). Prior to the high-resolution imaging, a CO molecule was picked up to the tip. The presence of the CO on the tip is confirmed by the characteristic low-energy IETS spectrum over the bare substrate, consisting of the frustrated translational (FT) and frustrated rotational (FR) modes located at ≈3 and

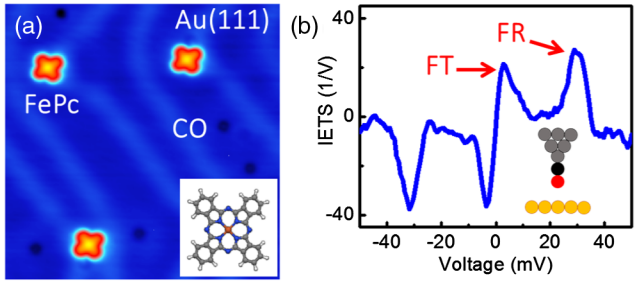

FIG. 1. Constant current STM images of FePc on Au(111) and IETS signal of a CO-functionalized tip. (a) 16×16 nm^2 constant-current STM image of the Au(111) surface and the coadsorbed CO and FePc molecules, acquired at the -200 mV and 10 pA set point. (b) STM-IETS of the CO adsorbed on the tip apex taken at the bare Au surface, showing the vibrational modes. The FR and FT modes of the CO are resolved. Bias voltage modulation was 3 mV at 963 Hz frequency. Stabilization set point $V = 50.0$ mV and $I = 3.0$ nA.

≈30 meV, respectively, as shown in Fig. 1(b). These values are similar to the previous IETS spectra of a CO molecule adsorbed on Ag(110) or Cu(111) [3,28,29]. In repeated attempts, we noticed that the amplitude and the shape of the FT peak in the IETS spectrum of the CO tip are very sensitive to the configuration of the metal tip apex before its functionalization [28]. For this reason, the metal apex preparation and CO picking process were repeated until an intense and regular IETS spectrum was obtained.

In Fig. 2(a) we present the maps of signals obtained while scanning with the CO-terminated tip in three constant heights above the molecule. These are the tunneling current I_t, frequency shift Δf, d^2I/dV^2, and its normalized value $(d^2I/dV^2)/(dI/dV)$, denoted in the following as STM, AFM, IETS, and norm. IETS, respectively. The bias voltage was set to 3 mV in order to optimize the sensitivity of the IETS signal to the peak corresponding to the FT vibrational mode. The STM contrast is dominated by a strong signal in the central part of the molecule, suppressing significantly the submolecular resolution of the molecule. We attribute the strong signal in the central part to d orbitals of Fe atom just below the Fermi level.

On the other hand, both AFM and IETS images exhibit sharp edges that reveal the backbone of the FePc molecule. At the closest distances the AFM contrast inverts and the contrast in the IETS map is enhanced. The $\Delta f(Z)$ spectroscopy shown in Fig. S1 [16] proves that the images were recorded at tip-sample separations where the repulsive interaction plays a dominant role. These observations are fully consistent with the assertion that the characteristic sharp edges in the AFM images are the direct consequence of the lateral bending of the CO due to the repulsive interaction [9]. Since the apparent positions of the sharp edges found in the IETS map correspond almost exactly to the AFM and STM images taken at the same moment, we can infer that the effect of CO bending indeed plays an

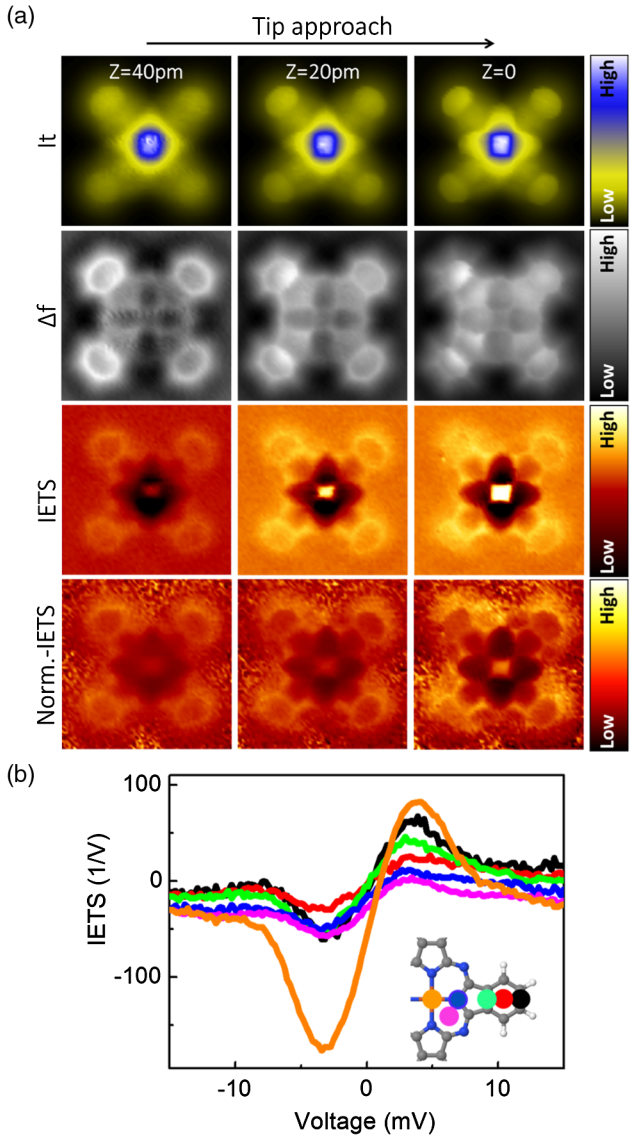

FIG. 2. Simultaneous AFM/STM/IETS images of FePc/Au(111) with a CO-functionalized tip and spatial variation of the FT mode. (a) Set of simultaneous (1.6×1.6 nm^2) current, Δf, IETS, and normalized-IETS constant-height images acquired at three different tip-sample distances with a CO decorated tip. The images were acquired with bias voltage of 3.0 mV. Both Δf and IETS images show the sharp edges related with the geometric structure of the FePc molecule. (b) Spatial dependence of the frustrated translational mode for the CO-functionalized tip above the FePc molecule.

indispensable role in the IETS imaging as it was predicted theoretically [10].

Next, we focus on the spatial variation of the FT signal over the FePc molecule. In their seminal work, Chiang *et al.* [3] performed spatially resolved IETS measurements at 600 mK above Co-phtalocyanine molecules. The high spectral resolution allowed them to resolve a subtle variation of the FT vibrational energy (frequency) and clearly showed a submolecular contrast. Later a

theoretical explanation of the imaging mechanism was suggested, based on the frequency change of the mode [10]. However, the IETS spectra acquired for the FT mode at various locations of the FePc molecule at 5 K, shown in the Fig. 2(b), reveal that the skeleton of FePc can be clearly resolved purely from variation of the amplitude of the IETS signal, even though variation of frequency cannot be directly observed due to broadening of the peak.

Remarkably, the highest amplitude is detected above the center of the FePc molecule, similarly to the STM dI/dV images. The IETS signal is expected to scale with the magnitude of the differential conductance dI/dV measured at the energy of the FT mode. Indeed, in the normalized IETS images $(d^2I/dV^2)/(dI/dV)$ the signal in the center is suppressed and the molecular structure is still clearly resolved although the normalization impairs the signal-to-noise ratio in the outer regions of the molecule.

For a further understanding of the origin of the contrast observed in the IETS images, we analyze the IETS signal at two different sites over one peripheral benzene ring of the FePc molecule. The spectra were acquired at constant height using the same parameters for the lock-in as during the IETS image acquisition. Figure 3(a) shows two IETS curves, obtained on a carbon bond (black) and at the center of the benzene ring (red) for comparison. The IETS shows a strong variation of the amplitude of the FT mode while the FR remains almost constant. This observation also documents that it is not possible to clearly resolve the molecular structure using the FR mode [3].

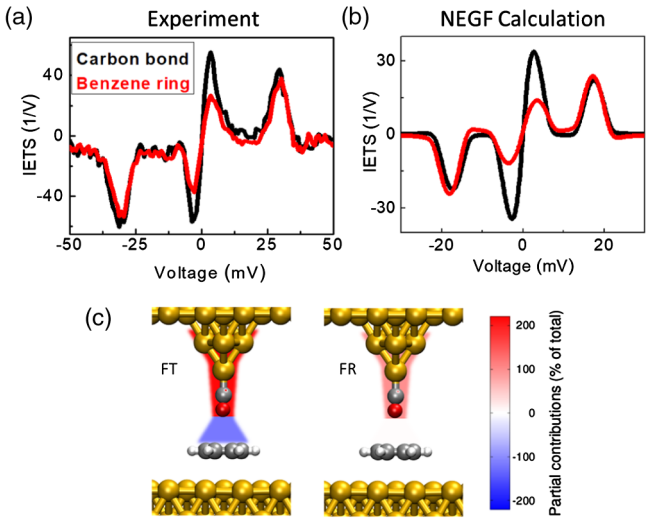

FIG. 3. Variation of IETS signal with tip position. Experimental (a) and calculated (b) IETS of the FT and FR modes above a carbon bond (black) and a benzene ring (red). Both experimental and calculated plots show the variation of the amplitude in the FT mode responsible for the IETS contrast. (c) Origin of the inelastic signal (as a fraction of the total inelastic amplitude) above the benzene ring. The signal for FR modes originates mainly in the CO and tip. However, for FT modes, the CO-benzene coupling also plays a significant role.

To get more insight into the imaging mechanism, we carry out first principles calculations of the inelastic signal on a simplified system consisting of a CO-functionalized tip placed above a benzene molecule. As we show below, this system is already sufficient to explain the experimental measurements. Details and methodology are given in Supplemental Material [16].

Figure 3(b) shows the calculated IETS spectrum for the CO-functionalized tip above a carbon bond and the benzene ring. Consistently with the experiments, the intensity of the calculated FT peak is reduced by a factor ~2, when going from the carbon bond to the benzene ring, while the intensity of the FR peaks is almost unchanged.

To understand why the inelastic signal of the FT modes changes strongly with tip position but not that of the FR modes, we analyze the different contributions that give rise to the inelastic peaks. The inelastic signal can be understood in terms of a Fermi golden rule involving the deformation potential and the left- and right-incident scattering states [30]. The use of a local-orbital basis enables us to group the contributions of the various regions of the junction where the inelastic signal is generated [31]. We consider a first set of contributions involving the CO molecule and the Au tip, and a second set consisting of the CO-benzene coupling (see [16] for details). The effect of the remaining terms is negligible. The modulus square of the sum of all contributions gives the calculated intensity of each inelastic peak.

These contributions for the most active pair of eigenchannels are shown in Fig. 3(c) for the CO-functionalized tip above the benzene ring. For clarity this is shown for only one FT and one FR mode but results are similar for all FT and FR modes on both configurations (details are given in Supplemental Material [16]). The boxes in Fig. 3(c) show the fraction of the total inelastic signal arising from each set of contributions: CO and tip, and the coupling of CO to the benzene substrate. The color scale quantifies the magnitude of each set of contributions relative to the total.

From the results shown above, we infer that there are clear differences in the origin of FT and FR modes. The FR mode is well described by the first set of contributions only. However, in order to properly capture the intensity of the FT mode, it is necessary to include these contributions as well as the off-diagonal terms between CO and benzene. Thus the inelastic signal of the FR mode is generated almost completely on the CO and tip alone, while that of the FT mode also involves the interaction with the benzene molecule.

The consequences of this localization of the inelastic signal are illustrated by constraining the dynamical region to just the C or O atom (see Supplemental Material [16]). When only the vibrations of the C atom are considered, the inelastic signal is unchanged with tip position. However, when only the O atom is allowed to vibrate, the calculated inelastic signal changes substantially from carbon bond to benzene ring positions. Thus the sensitivity of the inelastic

peaks to the interaction with the molecular substrate rests on the composition of the vibrational modes of CO. In FR modes the larger displacement corresponds to the C atom, close to the tip. In FT modes, on the other hand, the displacement is larger on the O atom, which, being closer to the benzene molecule, is more affected by the interaction with the molecular substrate. The higher sensitivity of FT modes to the position of CO above the molecule follows intuitively from this result.

To describe the variations of the IETS amplitude of the FT mode, we extend the fast PP-IETS method to calculate IETS maps [10]. We carry out an approximation of the perturbative inelastic transport theory [30] and consider that the IETS signal is proportional to two terms only: (i) Variation of the tunneling hopping T_{mn} between the electronic states of the tip (m) and of the sample (n) with respect to displacement of PP along vibration eigenmode $\mathbf{v}_\lambda$, and (ii) a prefactor depending on the energy of the vibrational mode ω_λ. Intuitively the prefactor represents the magnitude of the CO displacement during vibration, which is prolonged as the vibration mode becomes softer due to concave potential over the bonds [10]. The full derivation of the approach can be found in Supplemental Material [16]. This approximation is justified by the NEGF analysis, which revealed dominant contribution of oxygen to the IETS signal of the FT mode [16]. Consequently, the IETS signal γ_{FT} of the FT modes is defined as follows:

$$\gamma_{\mathrm{FT}} \sim \sum_{\lambda,m,n} C \frac{1}{\omega_\lambda M_{\mathrm{PP}}} \left| \frac{\partial T_{mn}}{\partial \mathbf{v}_\lambda} \right|^2, \qquad (1)$$

where C is a constant and M_{PP} the effective PP mass [16]. The vibrational mode λ goes over two FT modes. This PP-IETS method was implemented into the PP-code allowing simulation of the HR-STM and AFM images [9–11]. The computational cost of IETS images using this method is similar to standard STM simulation. The calculation of the high-resolution AFM/STM/IETS images relies on atomic and electronic structure of the adsorbed molecules on the surface. Therefore, we performed total energy DFT simulations of FePc molecule on an Au(111) surface with the FHI-Aims code [32] using the Perdew-Burke-Ernzerhof functional [33] and Tkatchenko-Scheffler vdW model [34] for geometry optimization. The electronic states used as input for PP-STM and PP-IETS codes were then calculated with the hybrid B3LYP functional [35] to provide better description of the metal-organic system.

Electronic states of the CO-functionalized tip were approximated by p_x, p_y, and s orbitals on the probe particle to represent π and σ conductance channels [11]. More details about parameters of the total energy DFT and PP-SPM simulations can be found in Supplemental Material [16].

Figure 4 shows the calculated high-resolution AFM, STM, and IETS images of the FePc molecule on the Au(111) surface for different tip-sample distances. The

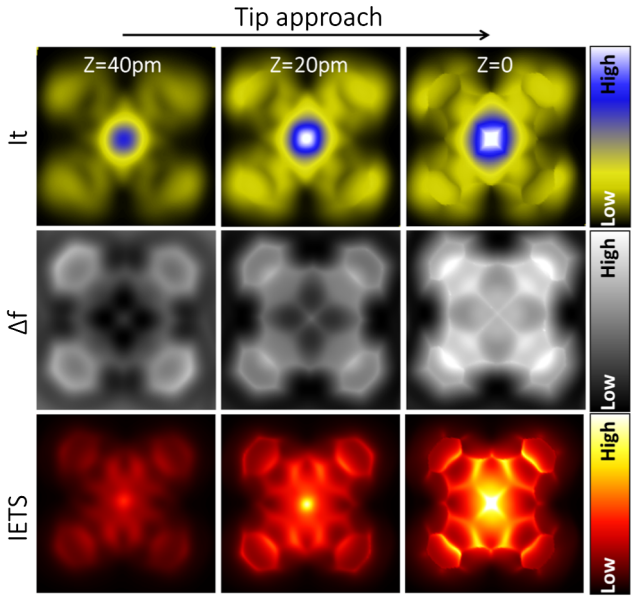

FIG. 4. Theoretical simulations of STM/AFM/IETS of FePc on the Au(111) surface at three different tip-sample distances. The tunneling current (top), Δf (middle), and IETS (bottom) images were calculated using the PP-SPM model.

simulated images capture well most of the characteristic features observed experimentally in all channels. In the STM mode, we are able to reproduce the dominant contrast observed in the center of the molecule, while a sharp contrast on external benzene rings is visible only in the close distance. On the other hand, the calculated STM images contain subtle submolecular features, which are not seen in the experiment. The AFM simulation reproduces very well both the characteristic sharpening of contrast and the contrast inversion at close distances. The only discrepancy consists of a missing rectangular feature in the center of the FePc molecule. We attribute these discrepancies to a peculiar charge distribution or structural relaxation between Fe and ligand, which is not described well within DFT approximation, or possibly to some chemical force between a CO tip and Fe atom that cannot be captured using a Lennard-Jones force field. The IETS channel resolves the molecular skeleton, with the characteristic bright spot in the center of the molecule in good agreement with the experimental evidence.

From PP-IETS simulations we can also analyze the influence of two contributions on the amplitude of the IETS signal (see Fig. S13 in [16]). We found that the prefactor $1/\omega_\lambda$ [Eq. (1)] is important only at close tip-sample distances due to fast decay of Pauli repulsion, which leads to concave curvature of interaction potential over the bonds. However, the molecular structure is resolved, both in the theory and experiment, over a range of $\approx$0.8 Å (see Fig. S1 in [16]). The IETS contrast at far distance is mainly caused by spatial variation of inelastic tunneling matrix element, as shown both by NEGF and PP-IETS simulations.

In conclusion, we demonstrated that the high-resolution IETS imaging with a CO-functionalized tip is feasible at 5 K with a spatial resolution superior to STM and comparable to AFM. Thus we believe that the IETS mode is promising for STM-only setups. The high-resolution contrast observed in all channels simultaneously demonstrates unambiguously the common imaging mechanism of the AFM/STM/IETS, related to lateral bending of the CO-functionalized tip. We provided detailed theoretical analysis of FT and FR vibrational modes showing their different localization in the STM junction. This explains why FT displays a large variation during scanning while FR is insensitive. This result opens the way to tune the surface sensitivity of the inelastic signal through appropriate molecular functionalization of the tip. We also showed that the submolecular contrast emerges not only from the changes of the CO vibrational frequency of the FT mode, but also due to the variation of the amplitude of the IETS signal. Finally, we extended accordingly the probe-particle AFM/STM/IETS model to include these two main ingredients necessary to reproduce the high-resolution IETS contrast.

We thank A. Peronio for fruitful discussions of the IETS signal. This research was financially supported by: the Czech Science Foundation (GACR) under Grants No. 15-19672S, No. 17-24210Y, the Purkyne Fellowship and Praemium Academiae program of the Academy of Sciences of the Czech Republic, and the European Union's Horizon 2020 research and innovation program under the Marie Sklodowska-Curie Grant No. 709114. The authors also acknowledge support from Ministry of Education, Youth and Sport of the Czech Republic (NanoEnviCz, Grant No. LM2015073, and Grant No. LO1305), Grant No. FP7 FET-ICT "Planar Atomic and Molecular Scale devices" (PAMS) project (funded by the European Commission under Contract No. 610446), Spanish Ministerio de Economia y Competitividad (MINECO) (Grant No. MAT2016-78293-C6-4-R), and the Basque Government (Dep. de Educacion and UPV/EHU, Grants No. IT-756-13 and No. PI-2016-1-0027). We thank CESNET Grant No. LM2015042 and CERIT Scientific Cloud Grant No. LM2015085, under the program "Projects of Large Research, Development, and Innovations Infrastructures" for computational resources.

*bdelatorre@fzu.cz
†jelinekp@fzu.cz

[1] R. Temirov, S. Soubatch, O. Neucheva, A. Lassise, and F. Tautz, New J. Phys. **10**, 053012 (2008).
[2] L. Gross, F. Mohn, N. Moll, P. Liljeroth, and G. Meyer, Science **325**, 1110 (2009).
[3] C. Chiang, C. Xu, Z. Han, and W. Ho, Science **344**, 885 (2014).
[4] L. Gross, N. Moll, G. Meyer, R. Ebel, W. Abdel-Mageed, and M. Jaspars, Nat. Chem. **2**, 821 (2010).
[5] B. Schuler, G. Meyer, D. Pena, O. Mullins, and L. Gross, J. Am. Chem. Soc. **137**, 9870 (2015).
[6] L. Gross, F. Mohn, N. Moll, B. Schuler, A. Criado, E. Guitian, D. Pena, A. Gourdon, and G. Meyer, Science **337**, 1326 (2012).
[7] D. de Oteyza, P. Gorman, Y.-C. Chen, S. Wickenburg, A. Riss, D. Mowbray, G. Etkin, Z. Pedramrazi, H.-Z. Tsai, A. Rubio, M. Crommie, and F. Fischer, Science **340**, 1434 (2013).
[8] P. Hapala, M. Švec, O. Stetsovych, N. van der Heijden, M. Ondracek, J. van der Lit, P. Mutombo, I. Swart, and P. Jelínek, Nat. Commun. **7**, 11560 (2016).
[9] P. Hapala, G. Kichin, C. Wagner, F. S. Tautz, R. Temirov, and P. Jelínek, Phys. Rev. B **90**, 085421 (2014).
[10] P. Hapala, R. Temirov, F. S. Tautz, and P. Jelínek, Phys. Rev. Lett. **113**, 226101 (2014).
[11] O. Krejči, P. Hapala, M. Ondráček, and P. Jelínek, Phys. Rev. B **95**, 045407 (2017).
[12] N. Moll, L. Gross, F. Mohn, A. Curioni, and G. Meyer, New J. Phys. **14**, 083023 (2012).
[13] S. K. Hämäläinen, N. van der Heijden, J. van der Lit, S. den Hartog, P. Liljeroth, and I. Swart, Phys. Rev. Lett. **113**, 186102 (2014).
[14] T. R. Albrecht, P. Grütter, D. Horne, and D. Rugar, J. Appl. Phys. **69**, 668 (1991).
[15] B. Stipe, M. Rezaei, and W. Ho, Science **280**, 1732 (1998).
[16] See Supplemental Material at http://link.aps.org/supplemental/10.1103/PhysRevLett.119.166001 for more details, which includes Refs. [17–26].
[17] L. Bartels, G. Meyer, and K. Rieder, Appl. Phys. Lett. **71**, 213 (1997).
[18] I. Horcas, R. Fernández, J. Gómez-Rodríguez, J. Colchero, J. Gómez-Herrero, and A. Baro, Rev. Sci. Instrum. **78**, 013705 (2007).
[19] W. L. Jorgensen and J. Tirado-Rives, J. Am. Chem. Soc. **110**, 1657 (1988).
[20] M. Brandbyge, J.-L. Mozos, P. Ordejón, J. Taylor, and K. Stokbro, Phys. Rev. B **65**, 165401 (2002).
[21] M. Dion, H. Rydberg, E. Schröder, D. C. Langreth, and B. I. Lundqvist, Phys. Rev. Lett. **92**, 246401 (2004).
[22] G. Foti, D. Sánchez-Portal, A. Arnau, and T. Frederiksen, Phys. Rev. B **91**, 035434 (2015).
[23] G. Román-Pérez and J. M. Soler, Phys. Rev. Lett. **103**, 096102 (2009).
[24] J. M. Soler, E. Artacho, J. D. Gale, A. García, J. Junquera, P. Ordejón, and D. Sánchez-Portal, J. Phys. Condens. Matter **14**, 2745 (2002).
[25] J.-T. Lü, R. B. Christensen, G. Foti, T. Frederiksen, T. Gunst, and M. Brandbyge, Phys. Rev. B **89**, 081405 (2014).
[26] J. Taylor, H. Guo, and J. Wang, Phys. Rev. B **63**, 245407 (2001).
[27] T. Frederiksen, M. Paulsson, M. Brandbyge, and A.-P. Jauho, Phys. Rev. B **75**, 205413 (2007).
[28] C. Xu, C. L. Chiang, Z. Han, and W. Ho, Phys. Rev. Lett. **116**, 166101 (2016).
[29] N. Okabayashi, A. Gustafsson, A. Peronio, M. Paulsson, T. Arai, and F. J. Giessibl, Phys. Rev. B **93**, 165415 (2016).

[30] M. Paulsson, T. Frederiksen, H. Ueba, N. Lorente, and M. Brandbyge, Phys. Rev. Lett. **100**, 226604 (2008).
[31] G. Foti and H. Vázquez, Phys. Rev. B **94**, 045418 (2016).
[32] V. Blum, R. Gehrke, F. Hanke, P. Havu, V. Havu, X. Ren, K. Reuter, and M. Scheffler, Comput. Phys. Commun. **180**, 2175 (2009).
[33] J. P. Perdew, K. Burke, and M. Ernzerhof, Phys. Rev. Lett. **77**, 3865 (1996).
[34] A. Tkatchenko and M. Scheffler, Phys. Rev. Lett. **102**, 073005 (2009).
[35] S. H. Vosko, L. Wilk, and M. Nusair, Can. J. Phys. **58**, 1200 (1980).

SUPPLEMENTAL MATERIAL

Submolecular resolution by variation of IETS amplitude and its relation to AFM/STM signal

Bruno de la Torre* and Martin Švec

Institute of Physics, Academy of Sciences of the Czech Republic, v.v.i., Cukrovarnická 10, 162 00 Prague, Czech Republic and Regional Centre of Advanced Technologies and Materials, Palacký University, Olomouc, Czech Republic.

Giuseppe Foti, Prokop Hapala, and Héctor Vázquez

Institute of Physics, Academy of Sciences of the Czech Republic, v.v.i., Cukrovarnická 10, 162 00 Prague, Czech Republic

Ondřej Krejčí

Institute of Physics, Academy of Sciences of the Czech Republic, v.v.i., Cukrovarnická 10, 162 00 Prague, Czech Republic and Charles University, Faculty of Mathematics and Physics, Department of Surface and Plasma Science, V Holešovičkách 2, 180 00, Prague, Czech Republic

Aran Garcia-Lekue and Thomas Frederiksen

Donostia International Physics Center (DIPC), Paseo Manuel Lardizabal 4, E-20018 San Sebastian, Spain and Ikerbasque, Basque Foundation for Science, 48013 Bilbao, Spain

Radek Zbořil

Regional Centre of Advanced Technologies and Materials, Palacký University, Olomouc, Czech Republic.

Andres Arnau

Donostia International Physics Center (DIPC), Paseo Manuel Lardizabal 4, E-20018 San Sebastian, Spain

Pavel Jelínek[†]

Institute of Physics, Academy of Sciences of the Czech Republic, v.v.i., Cukrovarnická 10, 162 00 Prague, Czech Republic

Regional Centre of Advanced Technologies and Materials, Palacký University, Olomouc, Czech Republic. and

Donostia International Physics Center (DIPC), Paseo Manuel Lardizabal 4, E-20018 San Sebastian, Spain

[*] corresponding author: bdelatorre@fzu.cz

[†] jelinkep@fzu.cz

I. EXPERIMENTAL METHODS

The experiments were carried out in a low-temperature STM/AFM with a qPlus tuning-fork sensor operated at 5 K (Createc Gmbh). A Pt/Ir tip mounted onto the sensor (resonant frequency $\approx$ 30 kHz; stiffness $\approx$ 1800 N/m) is oscillated with a constant amplitude 50 pm. A single crystal Au(111) sample (Mateck) was cleaned by several sputtering and subsequent annealing cycles in ultra-high vacuum. Iron (II) phthalocyanine (FePc) (Sigma Aldrich, Dye-content $\approx$ 90) was thermally evaporated from a Ta pocket onto the surface, which was kept at room temperature. The prepared system was transferred to the microscope, cooled down below 10 K and exposed to 1×10^{-8} mbar of CO gas during 10 seconds. For the spectroscopic measurements, both dI/dV and d^2I/dV^2 (i.e. IETS) were acquired with conventional lock-in technique with a modulation of 3 mV at a frequency of 963 Hz from the 1^{st} and 2^{nd} harmonics respectively. Typically one image point has been acquired in 200 ms, i.e. an image of 96×96 point in about 30 min. IETS spectra were acquired with same parameters used in image acquisition and corresponds with the average of 10 measurements. Remarkably, the images showed in the main text corresponds with raw data acquired directly from the 2^{nd} harmonic output of the lock-in. The tip was gently indented into the metal substrate (up to 1 nm) in order to prepare an apex suitable for picking up a CO molecule [1] from the substrate before the IETS measurements. All images were analyzed using WSxM software [2].

II. TIP-SAMPLE HEIGHT AND HIGH-RESOLUTION IETS CONTRAST

The dependence of the submolecular contrast in IETS images with the tip height, is shown in Fig. S1. At left, we plotted Δf(Z) spectroscospy above an outer carbon bond, a hexagon and the center of the FePc molecule. In the right panel, we displayed IETS and Δf images for three different heights (1), (2) and (3). In (1) the CO-tip begins to explore the repulsive interacting regimen and the submolecular contrast arises in both frequency shift and IETS images. In (2), the tip is approached 40 pm towards the surface. At this height, the IETS image reproduces the skeletal of the FePc molecule in good agreement with the Δf image. In (3), the tip is approached from (2) 40 pm towards the surface with an increase of the submolecular contrast in IETS image.

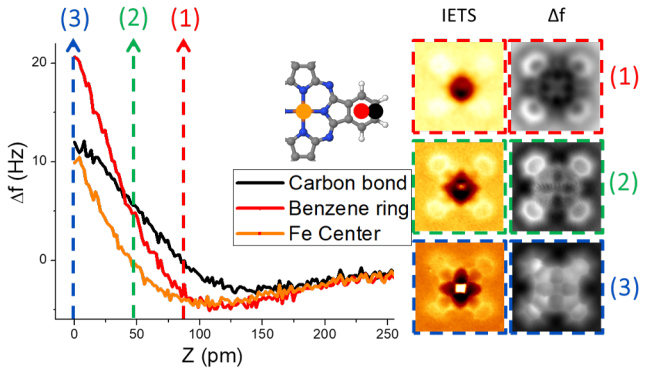

FIG. S1. **Tip height for submolecular contrast in IETS and frequency shift images.** At left Δf(Z) spectroscopy above an outer carbon bond, a hexagon and the center of the FePc molecule are plotted. At right, constant height IETS and Δf images are displayed for heights labeled as (1), (2) and (3) in the Δf(Z) spectroscopy. The IETS submolecular contrast arise in the repulsive regime.

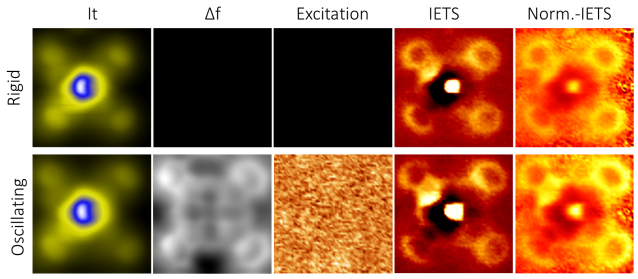

FIG. S2. **Comparison of IETS mapping with rigid and oscillating tip.** The molecule and the tip termination are the same in both cases.

III. HIGH-RESOLUTION IETS CONTRAST WITH STATIC AND OSCILLATING TIP

The dependence of the submolecular contrast in IETS images with the oscillation of the tip, is shown in Fig. S2. There, the tunneling current, frequency shift, Excitation, IETS and Norm.-IETS images of a FePc molecule with a static (top) and dynamic (down) tip are shown. IETS maps exhibit almost the same submolecular contrast for both the static and oscillating tip. The very similar contrast remarks the relevance of the method to resolve the molecular structure when only STM is possible

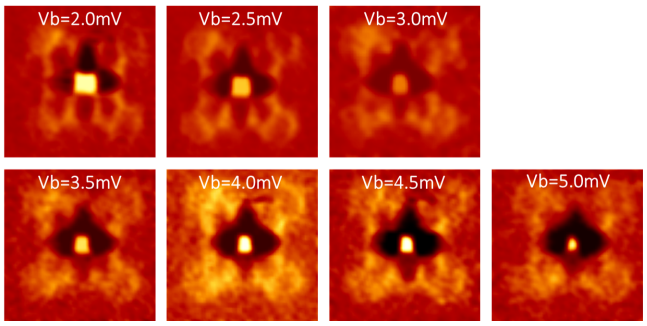

FIG. S3. **IETS bias dependence.**IETS images show su-molecular contrast in the range 2-5mV. The better spatial resolution is achieved for an energy close the FT mode

IV. HIGH-RESOLUTION IETS CONTRAST VS BIAS VOLTAGE

As the IETS image maps variation in the amplitude of the FT mode, the submolecular contrast should strongly depend on the applied bias voltage. This dependence is shown in Fig. S3 where the high-resolution IETS images are displayed at different bias voltages from 2 to 5 meV. While all images shown submolecular features, the ones observed around 3meV are sharper. This verify that, in our experimental performance the sub-molecular contrast can be achieved in a small range of energies, showing better spatial resolution for the energy of the FT mode.

V. COMPUTATIONAL DETAILS OF NEFG-DFT CALCULATIONS ON BENZENE ON AU(111) WITH CO-TERMINATED GOLD TIP

We performed first principles calculations based on density functional theory (DFT) Siesta [3] and nonequilibrium Green's function formalism (NEGF) [4, 5] of the electronic and inelastic transport properties of the system under study. In order to make the computational cost of the calculation feasible, we considered as a model system a benzene molecule adsorbed over an Au(111) substrate (Fig. S4). The top contact is formed by a pyramidal Au tip with a CO molecule vertically adsorbed on it. We believe this model provides a reliable picture of the electronic and inelastic transport properties of the system considered. Top panels in Fig. S4 show the side view of the geometries in the carbon bond [Fig. S4 a)] and benzene ring position [Fig. S4 b)]. The bottom panels in Fig. S4 show the top view of the benzene molecule over the first Au layer. The red dot represents the oxygen atom. Due to

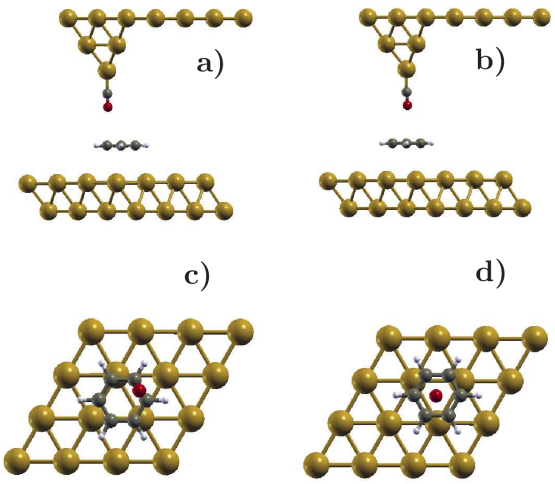

FIG. S4. Top panels: side view of the geometries on a) carbon bond and b) benzene ring configuration. Bottom panels: top view of the c) carbon bond and d) benzene ring geometries. The red dot represents Oxygen atom on the tip.

the use of periodic boundary conditions in these DFT calculations, it is not possible to place the tip at every x, y coordinate in real space. Instead, we choose to rigidly shift the benzene molecule under the tip to have the CO molecule on a carbon bond [Fig. S4 c)] or benzene ring [Fig. S4 d)] position with respect the underlying benzene.

We use SIESTA [3] and TRANSIESTA [5] for the structure relaxation and the calculation of the electronic and transport properties. We use a single$-\zeta$ plus polarization basis for bulk Au atoms and a double$-\zeta$ plus polarization basis for oxygen, hydrogen, carbon atoms and the surface Au atoms. Exchange-correlation energy is described by the van der Waals functionsl [6] as implemented in [7]. Geometry was relaxed till forces where below 0.01 eV/Å.

To verify that the rigid shifts of the benzene molecule do not introduce any artifacts, we calculate the projected density of states (PDOS) of the benzene molecule adsorbed on different positions over the Au(111) surface. Fig. S5 shows the PDOS for four adsorption geometries (shown in panel b). The PDOS curves are very similar regardless of the position or orientation of benzene over the Au surface. This suggests that the effect on the IETS spectra is minor.

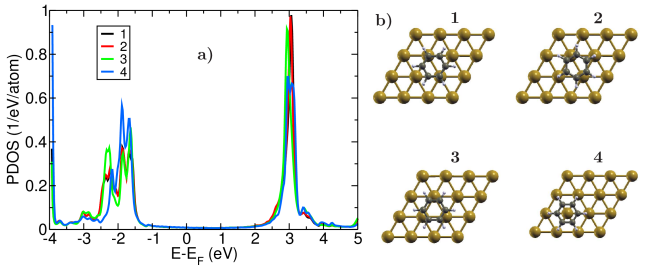

FIG. S5. Projected density of states (PDOS) of the benzene molecule for different adsorption geometries.

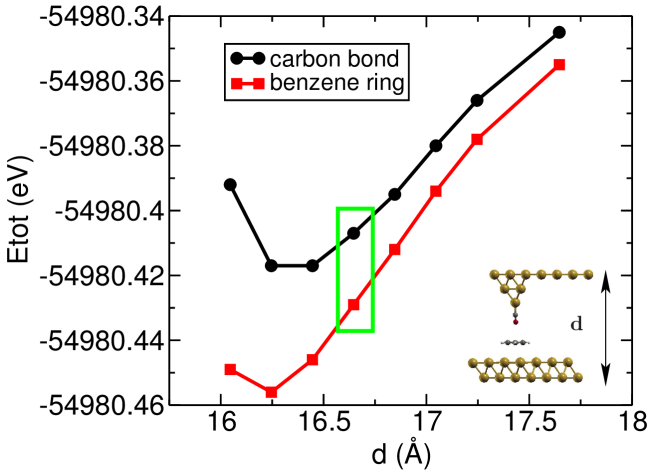

FIG. S6. Total energy as a function of electrode separation above a carbon bond and the benzene ring. The inset shows the inter-electrode separation d. The green rectangle encloses the energy points corresponding to the two geometries for which the inelastic spectra are calculated.

Fig. S6 shows the total energy as a function of inter-electrode separation above a carbon bond and the benzene ring. When the tip approaches the sample in the centre of benzene ring it experiences a more attractive force than a carbon bond. The green rectangle encloses the energy points corresponding to the two geometries for which the IETS was calculated.

For the calculation of the electron-vibration coupling matrix we use the INELASTICA code [8] with the $\mathbf{M}(\Gamma)$ approximation [9] in which one calculates the electron-vibration coupling matrix $\mathbf{M}$ in just one point of the Brillouin zone (Γ) for both electrons and phonons. The dynamical region includes the C and O atoms which gives six vibrational modes, two of which are degenerate frustrated translation modes and two degenerate frustrated rotational modes. Fig. S7 a)-d) and Fig. S8 a)-d) show the side and top view of the FT and FR

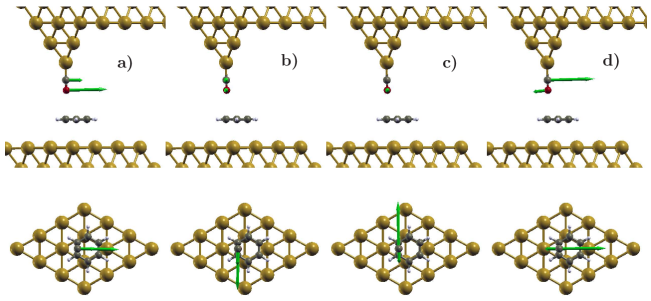

FIG. S7. Vibrational modes above carbon bond: a) FT1, b) FT2, c) FR1 and d) FR2.

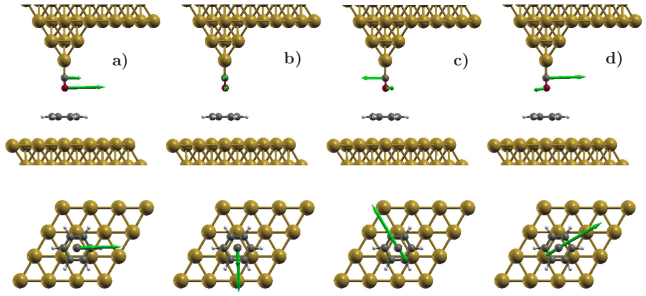

FIG. S8. Vibrational modes above benzene ring: a) FT1, b) FT2, c) FR1 and d) FR2.

modes on the carbon bond and on benzene ring sites, respectively. The inelastic electron tunneling spectra (IETS) are calculated over a k grid of 13×13 points in the Brillouin zone using the wide-band approximation (WBA) [8] with a modulation voltage of 3 mV in order to mimic the experimental performance. The WBA consists on evaluating the Green's functions, spectral functions and self-energies at the Fermi level. This approximation is justified if the electronic structure near the Fermi level has a smooth energy dependence in the energy range of vibrational excitations. In our case, both FT and FR are low-energy modes and therefore span a small energy range close to the Fermi level. The accuracy of the wide-band limit (WBL) is confirmed by comparing with calculations including the full energy dependence of the electronic structure (Fig. S9)[10].

A. Local contributions to the inelastic signal

The inelastic scattering of tunneling electrons due to localized molecular vibrations can be expressed in the form of a Fermi golden rule where the electron-vibration coupling matrix

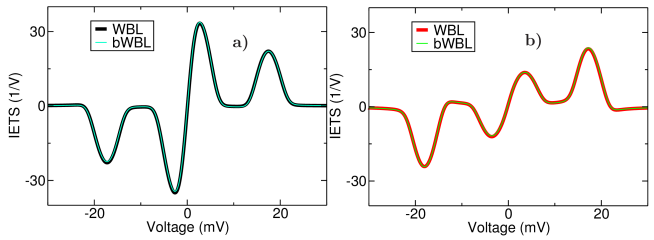

FIG. S9. IETS spectra above the a) "carbon-bond" and b) "benzene ring" calculated in the WBL and including the energy dependence of the electronic structure ("beyond WBL" or bWBL).

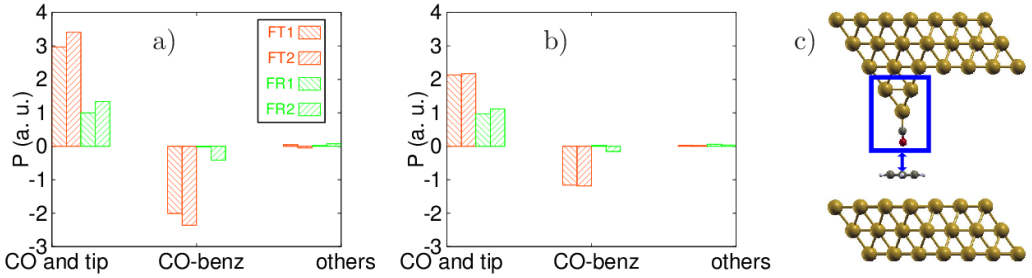

FIG. S10. Contributions to the most intense inelastic signals associated to the FT and FR modes on a) carbon bond and b) on benzene ring. The first term on the x axis represents the contributions generated in the region of the junction containing the Au atoms forming the pyramidal tip and the CO atoms; the second contribution represents the coupling between CO and benzene molecule while the last term are all other contributions. Panel c) shows a side view of the geometry where a blue rectangle encloses the region of the junction where the "CO and tip" term is calculated while the double-headed arrow represents the "CO-benz" coupling.

couples the states propagating from the left and right electrode [11]:

$$\gamma_{\lambda}^{FGR} = \sum_{m,n} \frac{4\pi e}{\hbar} |\langle \Psi_L^m | M_{e-ph}^{\lambda} | \Psi_R^n \rangle|^2, \tag{S1}$$

where $\Psi_{L(R)}^n$ are the left (right) eigenchannels and M_{e-ph}^{λ} is the electron-phonon coupling matrix associated to vibrational mode λ. When represented in a localized basis set this expression can be decomposed such to group the fraction of the total signal coming from a specific subset of atoms [12]. We thus define the following ratio:

$$P_{m,n}^{\lambda} = \frac{\sum_{i,j} \langle \Psi_{L,i}^m | M_{e-ph,i,j}^{\lambda} | \Psi_{R,j}^n \rangle}{\langle \Psi_L^m | M_{e-ph}^{\lambda} | \Psi_R^n \rangle}, \tag{S2}$$

where the indexes i, j run over the atomic orbitals of a pair of atoms. Here, we focus our analysis on the frustrated translation (FT) and frustrated rotation (FR) modes and identify

two main contributions: one coming from the region of the junction containing the terminal Au atoms of tip forming the pyramid and the CO atoms, and one from the coupling between CO atoms and the benzene molecule. Fig. S10 shows the term in Eq. S2 for the most intense inelastic transition (that is a pair n, m of eigenchannels for a given vibrational mode λ) for the bridge [Fig. S10 a)] and hollow [Fig. S10 b)] geometries, respectively. Panel c) in Fig. S10 shows a side view of the junction where a blue rectangle defines the region of the junction where the "CO and tip" contribution is calculated while the blue arrow represents the CO-benzene coupling to which the "CO-benz" contribution is associated. First one can see that, for each mode and geometry, the sum of the first two contributions makes the ratio in Eq. S2 very close to one which means that these terms account for most of the inelastic signal. Secondly, for the FR modes, the contribution generated on the tip approaches unity and is sensibly larger than the other two contributions which means that the inelastic peak associated to the FR mode is almost completely generated on the tip. In the case of the FT mode the situation is more complex. The contributions associated to the tip atoms and to the CO-benzene coupling have both a relatively strong amplitude and different sign which means that they should both be considered in order to correctly reproduce the amplitude of the total signal.

B. Quantifying the effect of localization of vibrational modes on the inelastic signal

In order to quantify the effect of localization of vibrational modes on the intensity of the inelastic signal we calculated the IETS for a model system where the dynamical region has been restricted to only one atom on the CO molecule. Fig. S11 shows the IETS calculated

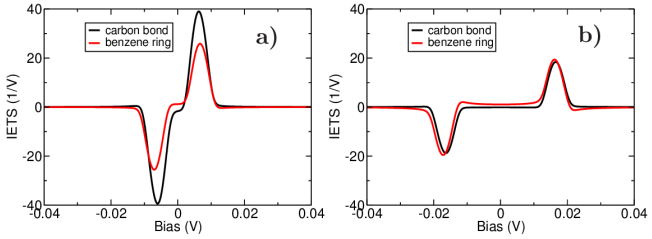

FIG. S11. IETS of the junction assuming only a) oxygen and b) carbon as dynamic atom.

assuming a) O and b) C as the dynamical atom. When the dynamical atom is carbon the amplitude of the corresponding IETS signal is basically independent of the position of the

tip [Fig. S11 b)]. When the vibrational mode is localized on the O atom, close to the benzene molecule, on the other hand, the IETS peak shows a strong decrease when moving the tip from the carbon bond to the benzene ring position [Fig. S11 a)]. This localization of the vibrational mode explains the qualitatively different behavior of the FT and FR mode. In the case of the FT mode in fact, the larger displacement vector is associated to the O atom while in the case of the FR to the C atom.

VI. DERIVATION OF APPROXIMATIVE METHOD TO CALCULATE IETS IMAGES

The inelastic transport in STM junction can be described using the Fermi golden rule [11] as discussed in the previous chapter, with Eq. S1. This expression for the inelastic scattering of tunneling electrons Eq. S1 can be rewritten in the following form [11]:

$$\gamma_{\lambda}^{\mathrm{FGR}} = \frac{e}{\pi\hbar}\mathrm{Tr}[M_{e-ph}^{\lambda} A_L M_{e-ph}^{\lambda} A_R], \tag{S3}$$

where $A_{L,R}$ represent spectral functions of left and right electrodes.

The electron-phonon coupling matrix M_{mn}^{λ} between states of the right and left electrode m, n can be written as:

$$M_{mn}^{\lambda} = \sum_{I,\nu} \langle m| \frac{\partial \widehat{H}_e}{\partial Q_{I\nu}} |n\rangle_{\mathbf{Q}=0} \mathbf{v}_{I\nu}^{\lambda} \sqrt{\frac{\hbar}{2M_I\omega_{\lambda}}}, \tag{S4}$$

where $\widehat{H}_e$ is single-particle electronic Hamiltonian, $\mathbf{Q}$ represents a displacement vector $\mathbf{Q} = \mathbf{R} - \mathbf{R_o}$ around equilibrium position $\mathbf{R_o}$ of atoms, indexes I and ν run over atoms and cartesian coordinates x, y, z, respectively; M_I means mass of atom I; ω_{λ} is the energy of given vibrational mode λ; $\mathbf{v}_{I\nu}^{\lambda}$ represents a vector of the atomic displacement of normal mode λ with eigenfrequency ω_{λ}. Indexes m, n represents the eigenstates of left and right electrodes propagating through the STM junction. The first term of Eq. S4 in the bracket is the response of the system to the vibrational modes, while the second term basically renormalises the inelastic signal γ by the frequency ω_{λ} of the given vibrational mode λ.

One of the key ingredients of the high-resolution imaging with functionalized tips is low reactivity of such tips, which allows stable scanning conditions in the repulsive regime. Typically, there is no chemical bond established between between CO-tip and a molecule

on surface. This means that the electronic states m, n do not change significantly while scanning. Consequently we can consider them constant. Second, the tunneling barrier between the functionalized tip and the sample causes, that the spectral functions A_L and A_R are localized mainly on the tip and sample, respectively. This leads to a suggestion that the states of the left electrode can be approximated as the states of the tip, while the states of the right electrode can be approximated as the states of the sample. The states m and n overlap only in the tunneling gap. Thus, the spectral function A_L now contain the information about the density of states of the tip ρ_T and about the eigenstates m, which are states of the tip only. The same works for A_R and density of states of the sample ρ_S and states n of the sample. With this consideration the trace from Eq. S3 can be simplified as $\sum_{mn} |\rho_T \rho_S M^{\lambda}_{mn}|^2$. Finally, the high-resolution IETS imaging is achieved via the variation of the FT mode. So we can restrict our simulation only to this mode. Due to a symmetry of binding configuration of CO molecule to the metal-tip base, there are two possible, mostly degenerated FT modes. The broadening of the IETS peaks is in our experimental setup much larger, than the difference between the FT energies. Therefore, the contributions from the both FT modes can be simply summed.

The expression of the inelastic signal γ_{FT} of the FT vibrational modes can be written:

$$\gamma_{FT} \sim \sum_{\lambda,m,n} C \frac{1}{\omega_\lambda} \left| \sum_{I,\nu} \langle m | \frac{\partial \widehat{H}_e}{\partial Q_{I\nu}} | n \rangle_{Q=0} \mathbf{v}^{\lambda}_{I\nu} \sqrt{\frac{1}{M_I}} \right|^2 , \tag{S5}$$

where C is a constant including constants from Eq. S1, Eq. S4 and an integration constant representing the density of state of the tip and the sample.

We choose to approximate the bracket in Eq. S5 as the change of tunnelling coupling between the tip and the sample - T_{mn} - along the the direction of the FT vibrational mode $\mathbf{v}_\lambda$. To stick with the PP formalism, we represent the tip (CO-tip) by the probe particle only - $m \in$ states of PP . The electronic states n are the states of the sample. Adopting this approximations, the IETS amplitude corresponding to the FT vibrational mode is then calculated as:

$$\gamma_{FT} \sim \sum_{\lambda,m,n} C \frac{1}{\omega_\lambda M_{PP}} \left| \frac{\partial T_{mn}}{\partial \mathbf{v}_\lambda} \right|^2 , \tag{S6}$$

where M_{PP} is an effective mass of the probe particle.

The T_{mn} from the Eq. S6 are identical with matrix elements T^{Chen} in our PP-STM approach, see ref. [13]. The partial derivative is performed numerically calculating the finite

differences of T_{mn} elements around the equilibrium point of the probe particle for given tip-sample position obtained from PP-AFM simulation.

VII. RELATIONSHIP WITH LOE-WBA FORMALISM

In this section we show that the result from the previous section, more precisely Eq. (S6), is exact to lowest order in the tunnel coupling matrix elements T_{ij}. For simplicity, let's consider the STM geometry with each side of the vacuum gap represented by one electronic level $\varepsilon_{S,T}$ hybridized by the interaction with the underlying metal electrode. This effective two-level system is coupled to a single vibrational mode with frequency ω_λ and normal mode Q representing the FT mode of the CO molecule on the tip apex. The Hamiltonian can be written as

$$\begin{aligned}\hat{H} = &\sum_{\alpha,\beta=S,T} H^0_{\alpha,\beta} d^\dagger_\alpha d_\beta + \sum_{\alpha=S,T}\sum_k (V_{\alpha,k\alpha} d^\dagger_\alpha c_{k\alpha} + \text{h.c.}) \\ &+ \sum_{\alpha,\beta} M_{\alpha,\beta} d^\dagger_\alpha d_\beta (b^\dagger_\lambda + b_\lambda) + \hbar\lambda\omega b^\dagger_\lambda b_\lambda \end{aligned} \tag{S7}$$

where d_α ($c_{\alpha k}$) is the fermionic annihilation operator in the device (lead) and b_λ the bosonic annihilation operator of the vibration. The bare Hamiltonian and the first-order electron-vibration coupling for the FT mode is given by

$$\mathbf{H}^0 = \begin{bmatrix} \varepsilon_S & T_{TS} \\ T_{TS} & \varepsilon_T \end{bmatrix}, \qquad \mathbf{M} = \frac{\partial \mathbf{H}^0}{\partial Q}\sqrt{\frac{\hbar}{2M_{\text{eff}}\omega_\lambda}} = \begin{bmatrix} 0 & \partial T_{TS}/\partial Q \\ \partial T_{TS}/\partial Q & \partial \varepsilon_T/\partial Q \end{bmatrix}\sqrt{\frac{\hbar}{2M_{\text{eff}}\omega_\lambda}} \tag{S8}$$

with M_{eff} the effective mass associated with the vibrational mode. Here we assumed that the FT mode is not perturbing the substrate level ($\partial\varepsilon_S/\partial Q = 0$).

The couplings $V_{\alpha,k\alpha}$ to the substrate and tip side electrodes give rise to level-broadening functions, which in the wide band limit (WBL) can be written as

$$\mathbf{\Gamma}_S = \begin{bmatrix} \Gamma_S & 0 \\ 0 & 0 \end{bmatrix}, \qquad \mathbf{\Gamma}_T = \begin{bmatrix} 0 & 0 \\ 0 & \Gamma_T \end{bmatrix}, \tag{S9}$$

According to the lowest order expansion (LOE) in the WBL limit [8], the vibrational signal amplitude in d^2I/dV^2 is proportional to the "symmetric" structure factor

$$\gamma^{\text{LOE}} = \frac{e}{\pi\hbar}\text{Tr}\left[\mathbf{G}^\dagger\mathbf{\Gamma}_S\mathbf{G}\{\mathbf{M}\mathbf{A}_T\mathbf{M} + \frac{i}{2}(\mathbf{\Gamma}_T\mathbf{G}^\dagger\mathbf{M}\mathbf{A}\mathbf{M} - \text{h.c.})\}\right] \tag{S10}$$

where $\mathbf{G} = [E_F\mathbf{1} - \mathbf{H}^0 + i(\mathbf{\Gamma}_S + \Gamma_T)/2]^{-1}$ is the bare Green's function evaluated at the Fermi energy E_F. Expanding in terms of the tunnel coupling T_{TS} one finds for this model that

$$\gamma^{\mathrm{LOE}} = \frac{e\rho_S(E_F)\rho_T(E_F)}{2\pi M_{\mathrm{eff}}\omega_\lambda}\left\{\left(\frac{\partial T_{TS}}{\partial Q}\right)^2 + \frac{2(E_F-\varepsilon_T)T_{TS}}{(E_F-\varepsilon_T)^2+(\Gamma_T/2)^2}\frac{\partial\varepsilon_T}{\partial Q}\frac{\partial T_{TS}}{\partial Q}\right\} + \mathcal{O}(T_{TS}^2) \tag{S11}$$

with

$$\rho_\alpha(E) = \frac{\Gamma_\alpha}{(E-\varepsilon_\alpha)^2+(\Gamma_\alpha/2)^2}, \qquad \alpha = T, S \tag{S12}$$

The vibrational signal amplitude in d^2I/dV^2 can often be well approximated by the phonon emission rate (Fermi Golden Rule) [11],

$$\gamma^{\mathrm{FGR}} = \frac{e}{\pi\hbar}\mathrm{Tr}\left[\mathbf{M}\mathbf{A}_S\mathbf{M}\mathbf{A}_T\right] \tag{S13}$$

which also reduces to

$$\gamma^{\mathrm{FGR}} = \frac{e\rho_S(E_F)\rho_T(E_F)}{2\pi M_{\mathrm{eff}}\omega_\lambda}\left\{\left(\frac{\partial T_{TS}}{\partial Q}\right)^2 + \frac{2(E_F-\varepsilon_T)T_{TS}}{(E_F-\varepsilon_T)^2+(\Gamma_T/2)^2}\frac{\partial\varepsilon_T}{\partial Q}\frac{\partial T_{TS}}{\partial Q}\right\} + \mathcal{O}(T_{TS}^2) \tag{S14}$$

Hence, within our model the two expressions Eqs. (S10) and (S13) are equivalent up to $\mathcal{O}(T_{TS})$.

VIII. SPM-DFT CALCULATIONS OF FEPC/AU(111) WITH CO-TIP

A. Total energy DFT calculations

Position of the molecule above the Au(111) substrate was obtained from a high resolution frequency shift image with the substrate registration as shown in Fig. S12 a). The geometry was optimized by means of the FHI-AIMS DFT package [14]. We used the PBE exchange-correlation functional [15] and three layered Au face-center-cubic (111) slab constructed from 6×6 super-cell and 35 Å of vacuum above. The Van der Waals interaction was applied via Tkatchenko-Sheffler method [16], the electronic calculation were spin-restricted and the first Brillouin zone was represented by a Γ-point only. The default "Light" basis set was used and all the Au atoms were fixed during the optimization. The geometry optimization was proceeded until the force criteria 0.01 eV/Å were reached.

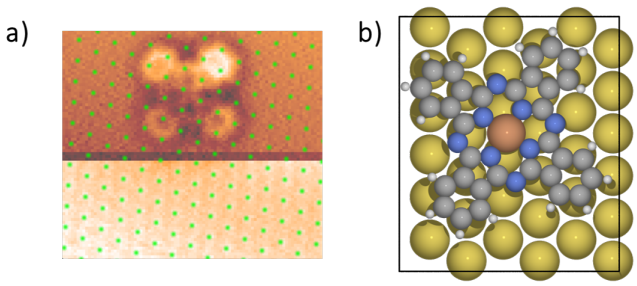

FIG. S12. **Adsorption geometry for the investigated FePc/Au(111).** a) high resolution Δf image of the FePc molecule and the Au(111) surface. b) DFT optimized geometry.

After the geometry optimization, the organic part of the FePc molecule is almost flat located 3.3 Å above the highest Au layer while the central iron atom is approximately 0.3 Å lower.

The Hartree potential and the electronic structure used as inputs in PP-AFM,PP-STM and PP-IETS calculations were obtained from a non-relaxing DFT calculation proceeded with the PBE-optimized geometry. In order to have more properly characterized electronic structure of the FePc molecule on the Au(111) surface, we applied hybrid B3LYP [17] exchange-correlation functional. Since these calculation are more computationally demanding only a single layer of gold could be applied. The super-cell used for the single point calculation is shown in Fig. S12 b).

B. PP-AFM calculations

The PP-AFM calculations were proceeded with the current version of the PP-AFM model [18, 19] with the probe particle parameters for an oxygen atom and the lateral stiffness of 0.24 N/m to simulate the flexible CO tip-apex. The L-J parameters for the H,C,N and Au were taken from the OPLS force-field [20]. In order to have better agreement with the experimental results we decreased the Fe atom Van der Waals radius to 2.1 Å, while the binding energy was taken from the standard force-field. We find the best agreement between theory and the experiment when we represent the charge on the probe particle by a quadrupole oriented in z-direction and the moment of -0.05×0.71^2 eÅ^2 with the negative charge occurring on the z-axis. The peak-to-peak amplitude for the F_z to Δf conversion was set to 1.0 Å. The simulations with these parameters are shown in Fig. 4 (middle) in

the main text. The closest simulated AFM image presented in the main manuscript was obtained with probe particle being placed 3.5 Å above the molecule. The other two images are simulated by 0.2 and 0.4 Å higher.

C. PP-STM and PP-IETS calculations

The PP-STM code [13] was extended including also d-orbitals could in the calculation of the tunnelling matrix elements T_{mn}. The formulas for the d-orbitals were derived in the same way as described in the original paper [13]. However, the d-orbitals decay faster into the vacuum then valence s and p-like orbitals. Thus the tunnelling matrix elements T_{mn} corresponding to d-orbitals are smaller. Since different DFT codes based on local basis sets have different decay of d-orbitals, we simply rescaled the contribution from the d-orbital by a factor of 0.2. Note, this number is approximately a proportion of the d-orbital vs. s-orbital FHI-AIMS radial function in the far distance used for the d-metals.

We calculate PP-IETS images using Eq. S6 with optimized position of the probe particle from PP-AFM simulations. The partial derivative of T_{mn} elements is performed numerically calculating the finite differences around the equilibrium point of the probe particle for given tip-sample position. We set the amplitude to be 0.05 Å. Nevertheless, we checked that the results are independent on the amplitude in range from 0.1 to 0.001 Å. The vibrational eigenenergies ω_λ and the eigenvectors are obtained by diagonalizing the dynamic matrix (Hessian) from the PP-AFM code as it was already proposed in ref. [19]. Since the whole CO molecule on the tip is in our model represented by the probe particle only, the dynamical matrix has dimension 3×3 corresponding to three eigenmodes. Two of them describe the FT mode of the CO, while the third one represents CO stretching mode, which has much higher energy. Therefore we do not consider the stretching mode in the PP-IETS calculations. We use the atomic mass of oxygen - 16 - as effective mass of the probe particle M_{PP} for the calculation of the frequencies [19]. Both the STM and IETS images were calculated using linear combination of p_x, p_y ($\approx$ 90 %) and s orbitals ($\approx$ 10 %) on the probe particle to achieve the best agreement with the experimental images.

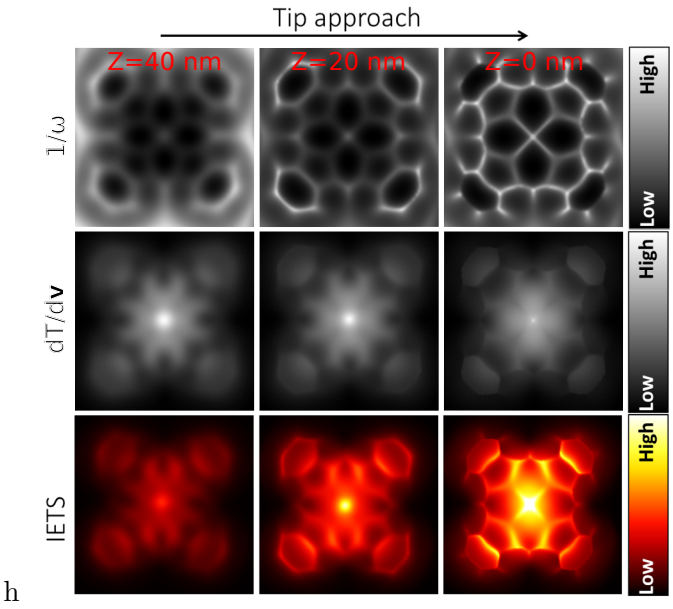

FIG. S13. **Parts of the simulated IETS contrast at three different tip-sample distances:** The part of the IETS signal coming from the rescaling prefactor - $\gamma_{prefactor}$ according to the Eq. S15 (top). The signal originating in the derivation of the tunnelling hopping according to the vibration - $\gamma_{derivative}$ from the Eq. S16 (middle). The full simulated IETS signal (bottom). The color-scale in each simulated image is normalized separately. The variation of the prefactor in the far distances is very small, therefore it has minor contribution to the full signal.

D. Parts of the IETS signal

In the last section we want to address, which part of the Eq. S6 is mostly responsible for the simulated IETS. We therefore separate the contributions from the rescaling factor γ_ω:

$$\gamma_\omega = \sum_\lambda C \frac{1}{\omega_\lambda M_{PP}}, \tag{S15}$$

and the derivative of the tunneling hopping $\gamma_{derivative}$:

$$\gamma_T = \sum_{\lambda,m,n} \left| \frac{\partial T_{mn}}{\partial \mathbf{v}_\lambda} \right|^2. \tag{S16}$$

According to the Fig. S13 it can be clearly distinguish that both parts contributes to the signal in the close tip-sample distance. While in the larger tip-sample distance the derivative

part γ_T is dominating in the contrast. (Please note, that $\gamma_{FT} \neq \gamma_\omega \times \gamma_T$.)

---

[1] L. Bartels, G. Meyer, and K. Rieder, Applied Physics Letters **71**, 213 (1997).

[2] I. Horcas, R. Fernández, J. Gómez-Rodríguez, J. Colchero, J. Gómez-Herrero, and A. Baro, Review of Scientific Instruments **78**, 013705 (2007), http://dx.doi.org/10.1063/1.2432410.

[3] J. M. Soler, E. Artacho, J. D. Gale, A. García, J. Junquera, P. Ordejón, and D. Sánchez-Portal, J. Phys.: Condens. Matter **14**, 2745 (2002).

[4] J. Taylor, H. Guo, and J. Wang, Phys. Rev. B **63**, 245407 (2001).

[5] M. Brandbyge, J.-L. Mozos, P. Ordejón, J. Taylor, and K. Stokbro, Phys. Rev. B **65**, 165401 (2002).

[6] M. Dion, H. Rydberg, E. Schröder, D. C. Langreth, and B. I. Lundqvist, Phys. Rev. Lett. **92**, 246401 (2004).

[7] G. Román-Pérez and J. M. Soler, Phys. Rev. Lett. **103**, 096102 (2009).

[8] T. Frederiksen, M. Paulsson, M. Brandbyge, and A.-P. Jauho, Phys. Rev. B **75**, 205413 (2007).

[9] G. Foti, D. Sánchez-Portal, A. Arnau, and T. Frederiksen, Phys. Rev. B **91**, 035434 (2015).

[10] J.-T. Lü, R. B. Christensen, G. Foti, T. Frederiksen, T. Gunst, and M. Brandbyge, Phys. Rev. B **89**, 081405 (2014).

[11] M. Paulsson, T. Frederiksen, H. Ueba, N. Lorente, and M. Brandbyge, Phys. Rev. Lett. **100**, 226604 (2008).

[12] G. Foti and H. Vázquez, Phys. Rev. B **94**, 045418 (2016).

[13] O. Krejči, P. Hapala, M. Ondráček, and P. Jelínek, Phys. Rev. B **95**, 045407 (2017).

[14] V. Blum, R. Gehrke, F. Hanke, P. Havu, V. Havu, X. Ren, K. Reuter, and M. Scheffler, Comput. Phys. Commun. **180**, 2175 (2009).

[15] J. P. Perdew, K. Burke, and M. Ernzerhof, Phys. Rev. Lett. **77**, 3865 (1996).

[16] A. Tkatchenko and M. Scheffler, Phys. Rev. Lett. **102**, 073005 (2009).

[17] S. H. Vosko, L. Wilk, and M. Nusair, Canadian Journal of Physics **58**, 1200 (1980), https://doi.org/10.1139/p80-159.

[18] P. Hapala, G. Kichin, C. Wagner, F. Tautz, R. Temirov, and P. Jelínek, Physical Review B **90**, 085421 (2014).

[19] P. Hapala, R. Temirov, F. Tautz, and P. Jelínek, Physical Review Letters **113**, 226101 (2014).

[20] W. L. Jorgensen and J. Tirado-Rives, J. Am. Chem. Soc. **110**, 1657 (1988).